(Received 9 September 2025, Accepted 31 October 2025, Scheduled 18 November 2025)

Study on the Spatiotemporal Characteristics of GICs in Shandong Peninsula, China under the Geomagnetic Storm of February 27, 2023

Xiaofeng Zhou[1], Xinwei Zhang[2], Xiaolong Li[3], Jia Cao[3], Tao Li[3], and Yanling Wang[3,*]

[1] *Department of Mechanical and Electrical Engineering, Weihai Vocational College, Weihai, Shandong, China*
[2] *State Grid Yantai Power Supply Company, Yantai, Shandong, China*
[3] *School of Airspace Science and Engineering, Shandong University, Weihai, Shandong, China*

ABSTRACT: For assessing Geomagnetically Induced Currents (GICs) risks in mid-latitude coastal power grids, this study developes a three-dimensional Earth conductivity model that incorporates coastal effects. The model was constructed using geological cross-sectional data from the China Earthquake Administration and measured terrestrial conductivity data. Focusing on the strong geomagnetic storm of February 27, 2023, the spatiotemporal characteristics of GICs in Shandong Peninsula across 34 substations and 46 transmission lines were accurately computed. The GICs peak of the substation appears at Muping, and GICs peak of the transmission line appears at Zouxian-Luzhou Line. Notably, two coastal substations exceeded the safety limit for GICs. Areas of highest risk are concentrated in the southeastern coastal region of Shandong, underscoring the significant impact of coastal effects and changes in geological structure. This method and its findings provide a global reference for predicting and issuing early warnings regarding GICs in long-distance mid-latitude coastal power grids.

1. INTRODUCTION

Currents in the Earth's magnetosphere and ionosphere, when being influenced by complicated solar plasma phenomena, can disturb the Earth's magnetic field. The Earth, acting as a conductor, generates induced ground electric fields in response to geomagnetic disturbances. Within closed circuits formed by transmission lines, transformer grounding points, and the Earth, GICs arise due to geomagnetic induction phenomena. This poses a threat to the safe and stable operation of power transformers and power systems [1–3].

During geomagnetic disturbances, GICs have been responsible for numerous incidents of transformer damage in high-latitude regions, at times leading to large-scale power outages [4]. In countries at mid-to-low latitudes, there have been incidents of GICs affecting power grids in recent years. These events are increasingly observed, particularly in coastal regions [5]. In contrast to earlier studies, which often simplified coastal induced ground electric fields as one-dimensional horizontal layers [6] or as simple two-dimensional sea-land boundary planes [7], thereby reducing solution accuracy. To address this, Liu et al. conducted comparative calculations of one-dimensional and three-dimensional induced ground electric fields in the Ling'ao coastal area [8, 9]. Building on this, Nakamura et al. established a three-dimensional ground conductivity model based on coastal effects for calculating induced ground electric fields [10]. However, these studies used idealized surface or line currents with fixed size and direction as excitation sources. In reality, geomagnetic disturbances generated by solar activity are the true "sources" that induce ground electric fields, and they are the fundamental drivers of GICs in power grids.

The geographical location of the Shandong Peninsula is of global significance, as it exhibits typical geological and topographical characteristics of mid-latitude coastal areas. In their study on GICs calculations for the region's power grid, Wang and colleagues computed the GICs for the 500 kV system in the Shandong Peninsula [3]. However, their approach still assumed fixed-size and direction ground electric fields as idealized excitation sources.

Recent studies have highlighted the importance of incorporating realistic conductivity structures and coastal effects into GICs modeling. Zhang et al. found that at three-block tectonic boundary zones, coast effects can systematically alter the direction of geoelectric field vectors and locally distort their magnitude, especially during geomagnetic storm pulses [11]. Marshalko et al. employed three-dimensional ground electric field modeling in Fennoscandia, demonstrating notable deviations from simpler models in coastal regions [12]. Wang and Zhang quantitatively analyzed two boundary configurations and confirmed that coastline geometry and seafloor depth exert a strong control on the intensity and distribution of geoelectric fields [13]. Hübert et al. proposed an improved ground electric field model [14], and Alves Ribeiro et al. demonstrated that the spatial resolution of conductivity models significantly affects GICs estimates [15]. Juusola et al. developed a three-dimensional approach for surface geoelectric fields [16]. These works provide essential context for the three-dimensional conductivity framework adopted in this study.

* Corresponding author: Yanling Wang (wangyanling@sdu.edu.cn).

To better align with real-world scenarios, this study departs from the conventional research practices involving ideal excitation sources in the investigation of induced ground electric fields and GICs. Instead, it establishes a comprehensive GICs calculation model encompassing the Earth's atmosphere, space, and ground. This study uses measured data from the geomagnetic storm of February 27, 2023, obtained through the Meridian Project (34.7°N, 118.4°E) [17]. It also incorporates geological cross-sections and ground conductivity measurements from the Shandong Peninsula. The real structure and parameters of the 500 kV power grid are taken into account. Using geomagnetic field variations generated by solar activity as the excitation source, the study examines the spatiotemporal distribution of induced electric fields and GICs. The results provide a physical basis for assessing the risk of GICs in the Shandong Peninsula power grid.

2. REAL-TIME SPACE WEATHER PARAMETER ACQUISITION AND MODELING

The Meridian Project is a significant technological infrastructure project for comprehensive monitoring of the space environment in the eastern hemisphere. The Meridian Project extends from 120°E in the north, starting from Mohe, passing through Shandong to the Antarctic Zhongshan Station, and from Shanghai in the east to near 30°N latitude in the west, reaching Lhasa. Currently, it comprises 15 monitoring stations. The Malingshan Station on the Shandong Peninsula is a crucial geomagnetic monitoring station within the Meridian Project, equipped with a fluxgate magnetometer and an inductive magnetometer. According to data from the Meridian Project Data Center, a strong geomagnetic storm event with Kp $=$ 7 and the equatorial geomagnetic index Dst $= -132$ nT occurred on February 27, 2023.

This study utilizes sampling data from the fluxgate magnetometer at the Malingshan Station. The raw data includes vertical component Z, horizontal intensity H, and magnetic declination D of the geomagnetic field. Through conversion formulas for geomagnetic components, the transformed data provides the eastward magnetic field intensity B_x, northward magnetic field intensity B_y, and vertical magnetic field intensity B_z during the occurrence of the geomagnetic storm, as shown in Fig. 1. The selected 600 seconds are from 2 : 22 PM to 2 : 32 PM (UTC) on February 27, 2023. The Malingshan Station shows that these 600 seconds are the period of most intense geomagnetic fluctuations on the Shandong Peninsula. The focus is to calculate GICs by developing a real three-dimensional Earth conductivity model that considers coastal effects. Therefore, the entire cycle including the initial phase, main phase, and recovery phase was not studied, but rather a relatively strong geomagnetic fluctuation period was studied for GICs calculation.

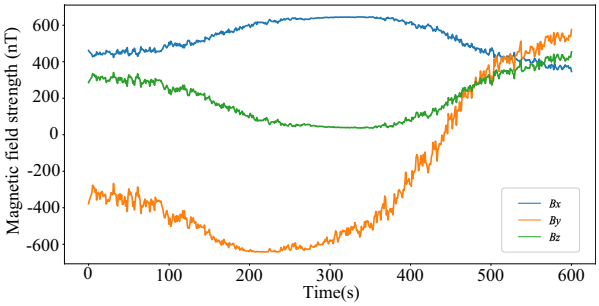

FIGURE 1. Change trend chart of the magnetic field of the Malingshan Observation Station in Shandong Peninsula of February 27, 2023.

3. THREE-DIMENSIONAL EARTH CONDUCTIVITY MODELING CONSIDERING COASTAL EFFECTS

The Shandong Peninsula is primarily located between 34°22′N and 38°24′N in latitude, and between 114°47′E and 122°42′E in longitude. In this study, we employed the geological cross-section diagram extending from Xiangshui, Jiangsu Province, to Mandula, Inner Mongolia Province, published by the Institute of Geology, China Earthquake Administration. In addition, geological structure stratification and terrestrial conductivity data from Shandong, as well as parts of Jiangsu and Hebei Provinces, were incorporated, as these regions may influence the induced geomagnetic field in the Shandong Peninsula. These datasets were used to construct terrestrial conductivity models. Fig. 2 presents the geological cross-section data and corresponding terrestrial conductivity for the Xiangshui-Si Shui in Jiangsu Province and Fucheng-Zibo in Shandong Peninsula, as adopted in this study. As for the areas adjacent to Shandong Peninsula, namely Henan and Anhui Provinces, modeling was based on the geological cross-section data from Fengxian, Shanghai, to Alashan, Inner Mongolia. In Fig. 2, the vertical axis represents depth (in kilometers), and the horizontal axis represents geographic location along the cross-section. The Moho boundary, which separates the crust from the upper mantle, is marked. The numbers within each layer correspond to the P-wave velocity (km/s), S-wave velocity (km/s), and rock density (g/cm^3). Green vertical curved line indicates highly conductive layers (S/m).

Due to variations in geological structures, the thickness of the Earth's crust and the magnitude of conductivity differ across various regions in Shandong. Additionally, factors such as soil moisture, proximity to the sea, etc., are taken into account. Shandong Peninsula's terrestrial areas are classified into seven geological zones: North Coastal Plain, East Hills, Southeast Hills, Jiaolai Plain, East Unstable Crust, Central-South Hills, and Southwest Coastal Plain. Using the Southwest Shandong Coastal Plain as an example, geological conductivity modeling is conducted based on the surveyed physical characteristics presented in Fig. 2.

The geological structure can be approximately divided into the upper crust (0–10 km below the surface), middle crust (10–25 km), lower crust (20–35 km), and lithospheric mantle (below 35 km). For the same geological region, the difference in Earth's conductivity models across different depths is approximately 0.1 S/m [18]. When modeling, it is practical to divide it into multiple layers. The North Shandong Coastal Plain and Southwest Shandong Coastal Plain have similar crustal structures, but due to different geographical locations, there is an approximate difference of 0.05 S/m in the conductivity between corresponding depths. However, as the regional span can reach hundreds of kilometers, Dimmock et al.'s research shows that

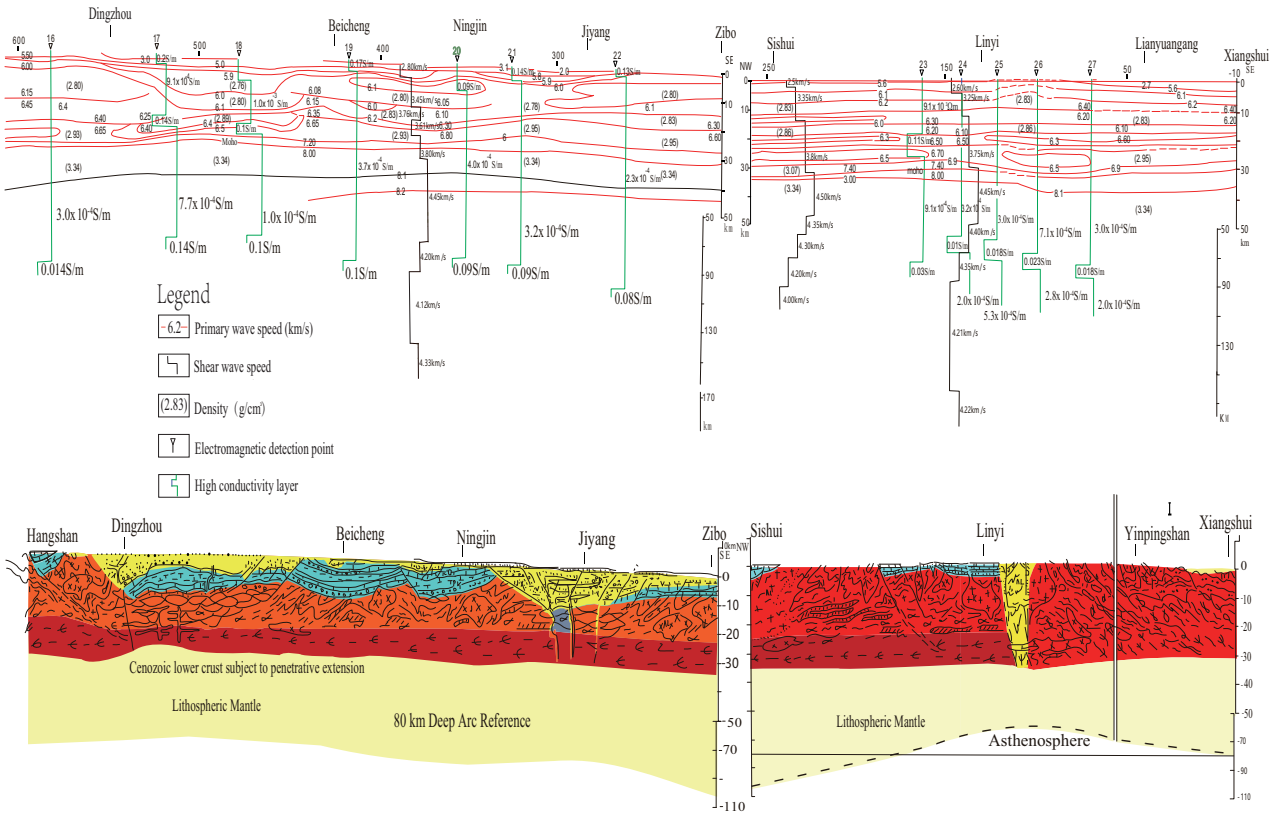

FIGURE 2. The 400 km vertical geological cross-section from Jiangsu Xiangshui to Shandong Sishui, and from Hebei Fucheng to Shandong Zibo.

regional variations in dB/dt and ground conductivity can have a significant impact on the final calculation of the induced geomagnetic field [19].

For modeling the conductivity in marine areas, we refer to Grayver's research and divided into two parts: seabed and seawater. The portion from sea level to a depth of 1 km is considered as seawater, and the part below 1 km is defined as seabed. The seabed can be approximated as an extension of the coastal terrestrial structure, using the conductivity structure of adjacent regions for modeling [20].

4. GEOGRAPHICAL LOCATION OF SHANDONG 500 KV POWER GRID

Due to distinct geological structures, the Shandong Peninsula is divided into 7 geological zones. Based on available information, the Shandong 500 kV power grid comprises a total of 34 substations and 46 transmission lines. The geological regions of the Shandong Peninsula and the geographical connections of the Shandong power grid are illustrated in Fig. 3. The power grid in Shandong exhibits a pattern of transmitting power from west to east, with the longest transmission line stretching to 173.8 km.

5. THREE-DIMENSIONAL CALCULATION MODEL

The three-dimensional terrestrial conductivity model of Shandong Peninsula and its surrounding areas, established based on the above-mentioned method, is depicted in Fig. 4(a). The model was developed using COMSOL Multiphysics and spans 730 km in the east-west direction, 460 km in the north-south direction, and extends vertically to 650 km below the ground surface. Due to the complex and relatively fast-changing dynamics of the solar wind-magnetosphere-ionosphere coupling process, ground-based magnetic data is utilized as the excitation for the model.

Building upon the terrestrial conductivity model shown in Fig. 4(a), real-time monitored spatial weather parameters are employed as additional stimuli. The influence of the solar wind on the induced geomagnetic field is represented by enclosing the three-dimensional terrestrial model of the Shandong Peninsula within a spherical air domain of 1000 km radius, as illustrated in Fig. 4(b).

6. THREE-DIMENSIONAL INDUCED GEOELECTRIC FIELD SIMULATION BASED ON FINITE ELEMENT METHOD

This article, in modeling and solving the induced geomagnetic field generated by geomagnetic disturbances, considers the following two hypothetical conditions:

(1) Modeling and analysis are conducted in a rectangular coordinate system, neglecting the Earth's rotation and curvature.

(2) It is assumed that the relative magnetic permeability is uniformly set to 1 throughout the entire solution domain [21].

Initially, the finite element method is employed to partition the solution domain into a mesh. Subsequently, sub-

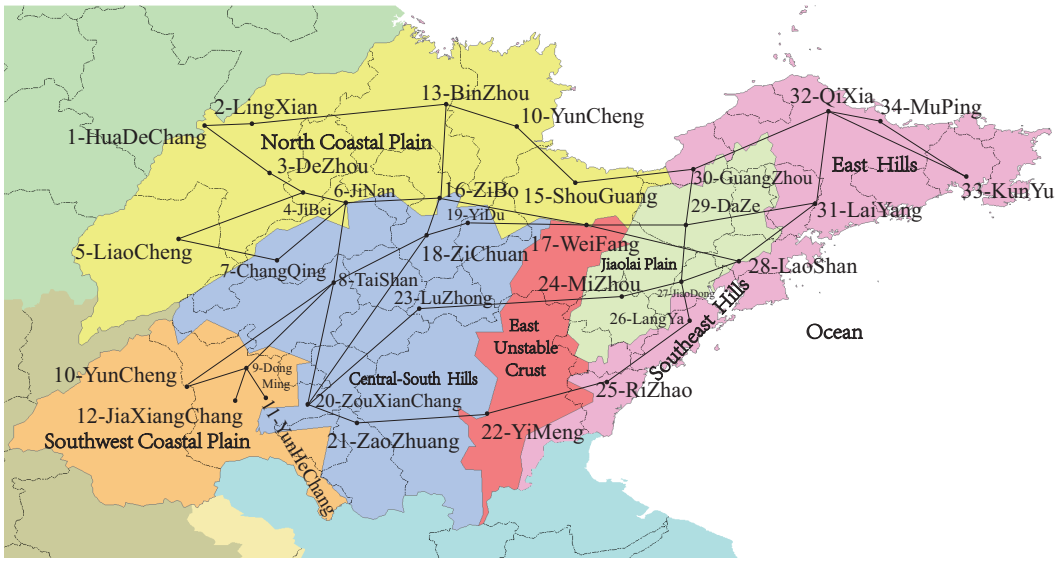

FIGURE 3. Shandong 500 kV power grid geographical location wiring diagram.

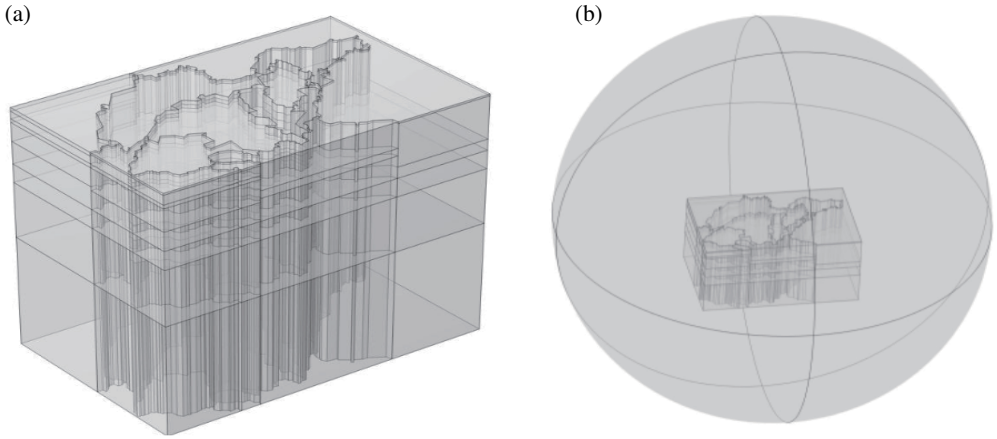

FIGURE 4. Three-dimensional models. (a) Geoelectric conductivity model of the shandong Peninsula. (b) Induced geoelectric field model.

elements are delineated based on the physical and medium properties of the electromagnetic field, as well as boundary constraints. Mesh refinement is applied at interfaces with significant conductivity variations, while regions with relatively uniform conductivity undergo sparse mesh partitioning. Based on Maxwell's equations, the fundamental equation for the three-dimensional induced geomagnetic field is derived as follows:

$$\frac{1}{\mu_0}\nabla\times\nabla\times\vec{A}+\sigma\left(\frac{\partial\vec{A}}{\partial t}+\nabla\varphi\right)=\vec{J}_s \tag{1}$$

$$\nabla\cdot\sigma\left(\frac{\partial\vec{A}}{\partial t}+\nabla\varphi\right)=0 \tag{2}$$

$$\vec{E}=-\left(\frac{\partial\vec{A}}{\partial t}+\nabla\varphi\right) \tag{3}$$

In the given equations, $\vec{J}_s$ denotes the spatial current source, which is effectively derived from space weather parameters; $\vec{A}$ represents the vector magnetic potential at individual nodes; φ stands for the scalar electric potential; operator ∇ is the standard gradient operator; μ_0 signifies the magnetic permeability; and σ denotes the electrical conductivity.

Considering the time-domain three-dimensional geomagnetic field boundary value problem in practical scenarios, solving Equations (1), (2), and (3) provides electric field $\vec{E}$ within the solution domain.

This study develops a time-domain transient model for the distribution of induced geoelectric fields, incorporating spatial weather parameters and accounting for electromagnetic wave attenuation. The model incorporates the amplitude and direction of the induced geoelectric field during the 600-second interval of the February 27, 2023 geomagnetic storm. The spatiotemporal distribution of the induced geoelectric field on the Shandong Peninsula during this geomagnetic storm is illustrated in Fig. 5. In Fig. 5, different colors are used to represent the magnitude of the induced geoelectric field, and

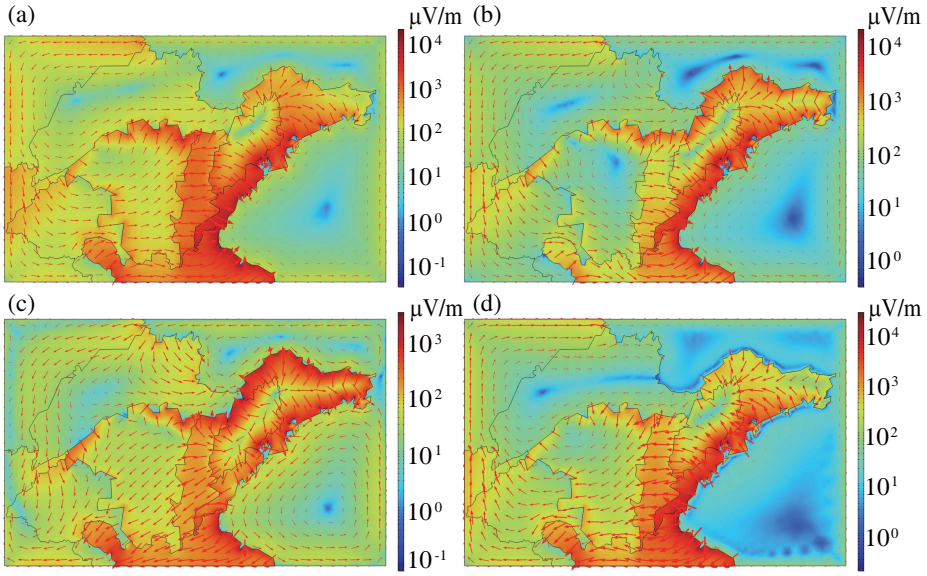

FIGURE 5. Electric fields in Shandong Peninsula and surrounding areas. (a) Electric fields at 100 s. (b) Electric fields at 200 s. (c) Electric fields at 300 s. (d) Electric fields at 400 s.

the arrows indicate the direction of the induced geoelectric field. Figs. 5(a), (b), and (d) show that at 100 s, 200 s, and 400 s, the areas of the Southeast Shandong Hills geological zone exhibit higher amplitudes of the induced geoelectric field. The calculated results for the amplitude of the induced geoelectric field show values that exceed approximately 1 V/km. In Fig. 5(c) at 300 s, areas with larger amplitudes of the induced geoelectric field are located between the East Shandong Hills geological zone and Southeast Shandong Hills geological zone. It is evident that the amplitude of the induced geoelectric field in coastal areas is significantly larger than that in inland areas [10]. The maximum induced field strength is mainly distributed in coastal bays, attributed to the more complex geological-electrical structure variations in coastal regions and the impact of coastal effects.

In inland areas of the Shandong Peninsula, larger induced geomagnetic fields are distributed in various regions within the central part of Shandong, often near the boundaries of areas with different geological structures. In summary, regions with larger induced geomagnetic fields are located at interfaces where the conductivity values on both sides differ significantly. The conductivity across these interfaces may differ by tens to hundreds of times. A larger conductivity contrast leads to stronger induced geomagnetic fields at those locations [22, 23].

At calculation moment of 100 s, 200 s, and 300 s, the direction of the induced geomagnetic field in coastal areas is mostly from inland towards the ocean. However, at 400 s, the direction of the induced geomagnetic field in coastal areas reverses, pointing from the ocean towards inland. Compared to the direction of the induced geomagnetic field at 100 s, there is a significant reversal in the direction of the induced geomagnetic field in most areas. In general, during this geomagnetic storm period, there is a noticeable change in the direction of the induced geomagnetic field in most areas of the Shandong Peninsula.

7. RESULTS

By incorporating geomagnetic field data, the calculation of GICs in the Shandong Peninsula 500 kV power grid using the Node Admittance Method reveals GICs values for each substation within 500 seconds [24]. At the 422nd second of the geomagnetic storm, the sum of the magnitudes of the GICs across all 34 transformers reaches its maximum. At this moment, all transformers reach their maximum reactive power loss. The entire 500 kV transmission system experiences the most severe voltage fluctuations, creating the highest risk of voltage instability.

Additionally, the maximum GIC values calculated for each station are depicted in Fig. 6(a), and the size and color of the circles together represent the size of the GICs at the substations. It can be observed that the maximum magnitude of GICs for substations in the Shandong 500 kV power grid ranges between 0.01 A and 41.44 A. Two substations, Qixia and Muping, located in coastal areas, exceed the allowable value of 30 A specified by the "High Impedance Grounding Device for HVDC Ground Electrode Systems". Their GICs magnitudes are 37.25 A and 41.44 A. Both Qixia and Muping substations are located exactly in this coastal zone. Because of the sharp conductivity contrast between seawater and continental crust, the induced field intensity is locally enhanced. This configuration results in larger grounding potential differences, amplifying the GIC inflow. The GICs values exceeding the permissible limit at these substations may lead to potential risks of transformer vibration, temperature rise, insulation aging, and other damages.

For the instantaneous values and the trend of GICs throughout the entire calculation period, the results for the maximum GICs value at Muping substation are presented in Fig. 6(b). Upon the observation of Fig. 6(b), the GICs values at Muping substation initially rise transiently from the initial state of

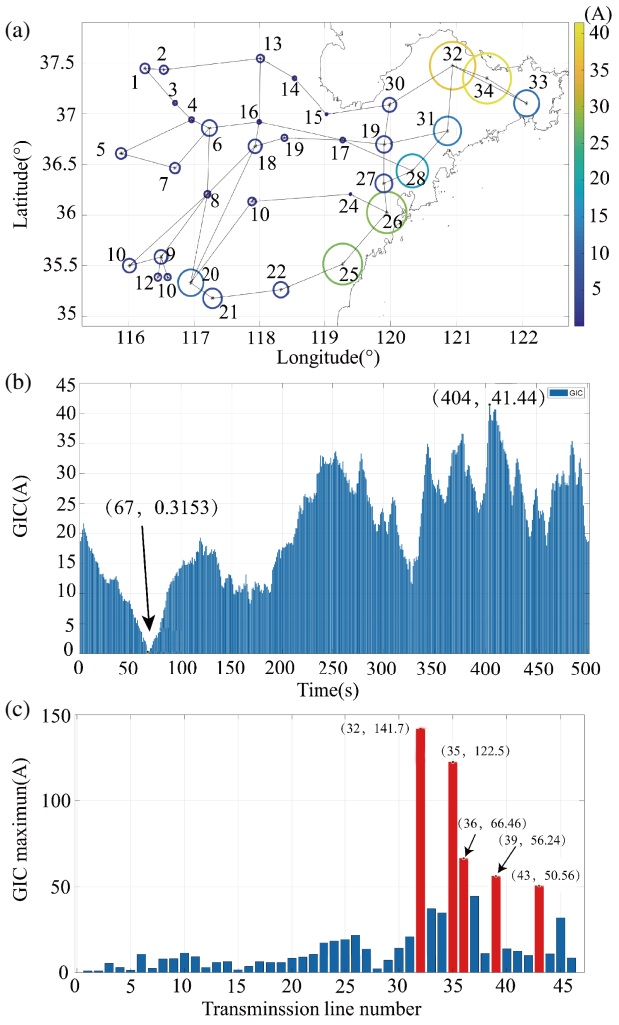

FIGURE 6. Shandong 500 kV power grid calculated GICs-related values. (a) Maximum GICs values of each substation. (b) GICs instantaneous values at Muping substation. (c) Maximum GICs values of each transmission line.

17.38 A to briefly exceed 20 A, followed by a gradual decrease. Subsequently, the trend of GICs exhibits periodic variations resembling a sine wave. The minimum GIC value occurs at the 67th second of the calculation, with a magnitude of 0.31 A, while the maximum value occurs at the 404th second, reaching 41.44 A.

In the calculation of GICs on transmission lines, the magnitudes of each component of the induced electric field are taken as the average values across various points along the line. The maximum GICs values for each transmission line in the Shandong 500 kV power grid are shown in Fig. 6(c). The maximum GICs values for most transmission lines in the Shandong Peninsula 500 kV power grid are predominantly below 50 A. However, there are five transmission lines with GICs exceeding 50 A: Zouxian-Luzhou, Luzhou-Mizhou, Jiaodong-Langya, Laoshan-Laiyang, and Guangzhou-Qixia mostly distributed in coastal regions. At the 476th second of the geomagnetic storm, the Zouxian-Luzhou transmission line reaches its maximum GICs magnitude of 141.7 A. At this moment, the risk of reduced measurement accuracy increases, and the likelihood of relay protection misoperation that could trigger chain reactions reaches its peak. This line is located in the hilly geological area of central and southern Shandong Province, with a complex geographical structure. The large GICs are the result of the combined effects of the direction and magnitude of the induced geoelectric field and established power grid structure.

Wang et al. assumed an induced electric field of 1 V/km. Among the 34 substations, 11 exhibited GICs exceeding 100 A, with 2 substations reaching GICs as high as approximately 200 A [3]. As shown in Fig. 5 of this study, regions with an induced geoelectric field greater than 1 V/km are extremely scarce. Consequently, the calculated values in this work are lower than those reported by Wang et al.

8. CONCLUSIONS

By referencing the geological cross-sectional data provided by the Geological Cloud website for Jiangsu Xiangshui, through Shandong to Inner Mongolia Mandula, and considering the influence of coastal effects, a three-dimensional terrestrial conductivity model for the Shandong Peninsula is established based on the actual geological structure and measured electrical conductivity data.

Throughout the entire period of the geomagnetic storm, the maximum amplitude of the induced geomagnetic field on transmission lines in the Shandong Peninsula reaches 4.32 V/km, and the direction of the induced geomagnetic field undergoes a noticeable reversal, indicating significant changes. The maximum value of GICs in the substation is 41.44 A, with two transformers exceeding the allowable safety value. The maximum value of GICs on transmission lines reaches 141.7 A. The Shandong Peninsula faces operational risks such as voltage fluctuations or instability, transformer damage, and misoperation of relay protection.

The regions with larger amplitudes of the induced geomagnetic field in the Shandong Peninsula are mainly located in the coastal areas of Southeast Shandong, where the complex variations in geological-electrical structures and the impact of coastal effects on field strength are evident. In most instances, the amplitude of the induced geomagnetic field in the coastal area south of Southeast Shandong is greater than that in the coastal area north of Northeast Shandong. It indicates that the different geological regions with varying terrestrial conductivity and the shape of the coastline in coastal areas also have a significant impact on the distribution of induced geomagnetic fields and GICs.

ACKNOWLEDGEMENT

This study was supported by Shandong Province Science and Technology Small and Medium-Sized Enterprises Innovation Ability Enhancement Project (2023TSGC0682) and Shandong Provincial Natural Science Foundation (grants No. ZR2023MD086).

REFERENCES

[1] Apatenkov, S. V., V. A. Pilipenko, E. I. Gordeev, A. Viljanen, L. Juusola, V. B. Belakhovsky, Y. A. Sakharov, and V. N. Se-

livanov, "Auroral omega bands are a significant cause of large geomagnetically induced currents," *Geophysical Research Letters*, Vol. 47, No. 6, e2019GL086677, 2020.

[2] Liu, C., Y. S. Ganebo, and D. Wang, "Optimal configuration method of capacitor isolation device against DC bias on improved niche GA algorithm," *The Journal of Engineering*, Vol. 2019, No. 16, 1571–1574, 2019.

[3] Wang, H., Z.-Y. Xing, N. Balan, Y.-L. Wang, Q.-H. Zhang, and L.-K. Liang, "Simulation and analysis of geomagnetically induced current levels in shandong power grid," *Space Weather*, Vol. 19, No. 4, e2020SW002615, 2021.

[4] Xu, W.-H., Z.-Y. Xing, N. Balan, L.-K. Liang, Y.-L. Wang, Q.-H. Zhang, Z.-D. Sun, and W.-B. Li, "Spectral analysis of geomagnetically induced current and local magnetic field during the 17 March 2013 geomagnetic storm," *Advances in Space Research*, Vol. 69, No. 9, 3417–3425, 2022.

[5] Liu, C. M., X. Wang, L. G. Liu, B. Dong, and Z. Z. Wang, "Calculation method of geomagnetically induced currents in the power grid considering the influence of the coast effect," *Proceedings of the CSEE*, Vol. 36, No. 22, 6059–6066, 2016.

[6] Honkonen, I., A. Kuvshinov, L. Rastätter, and A. Pulkkinen, "Predicting global ground geoelectric field with coupled geospace and three-dimensional geomagnetic induction models," *Space Weather*, Vol. 16, No. 8, 1028–1041, 2018.

[7] Pulkkinen, A., M. Hesse, M. Kuznetsova, and L. Rastätter, "First-principles modeling of geomagnetically induced electromagnetic fields and currents from upstream solar wind to the surface of the Earth," *Annales Geophysicae*, Vol. 25, No. 4, 881–893, 2007.

[8] Liu, L. G., P. H. Yang, S. X. Guo, C. M. Liu, and C. L. Ma, "Impact of geoelectric field direction and AC system structure on geomagnetically induced currents in ±800 kV Mengxi convertor station," *Power System Technology*, Vol. 40, No. 5, 1295–1300, 2016.

[9] Liu, C. M., C. X. Lin, X. N. Wang, X. Li, and W. Li, "Influence of coast effect on geomagnetically induced currents in power grid," *Power System Technology*, Vol. 41, No. 8, 2716–2722, 2017.

[10] Nakamura, S., Y. Ebihara, S. Fujita, T. Goto, N. Yamada, S. Watari, and Y. Omura, "Time domain simulation of geomagnetically induced current (GIC) flowing in 500-kV power grid in Japan including a three-dimensional ground inhomogeneity," *Space Weather*, Vol. 16, No. 12, 1946–1959, 2018.

[11] Zhang, X., A. D. Santis, L. Perrone, and X. Wu, "A similar coast effect of geoelectric field directions in a three-block boundary zone during geomagnetic storm pulses," *Geophysical Journal International*, Vol. 241, No. 3, 1936–1946, 2025.

[12] Marshalko, E., M. Kruglyakov, A. Kuvshinov, and A. Viljanen, "Three-dimensional modeling of the ground electric field in fennoscandia during the halloween geomagnetic storm," *Space Weather*, Vol. 21, No. 9, e2022SW003370, 2023.

[13] Wang, X. and S. Zhang, "The geoelectric field coast effect: Results from two dimensional finite element method and analytic solutions," *Alexandria Engineering Journal*, Vol. 77, 525–536, 2023.

[14] Hübert, J., E. Eaton, C. D. Beggan, A. M. Montiel-Álvarez, D. Kiyan, and C. Hogg, "Developing a new ground electric field model for geomagnetically induced currents in britain based on long-period magnetotelluric data," *Space Weather*, Vol. 23, No. 8, e2025SW004427, 2025.

[15] Alves Ribeiro, J., F. J. G. Pinheiro, R. R. Santos, and M. A. Pais, "Effect of spatial resolution of conductivity models for Geomagnetically Induced Currents estimation: case study in a geological complex region," *Geophysical Journal International*, Vol. 242, No. 3, ggaf277, 2025.

[16] Juusola, L., H. Vanhamäki, E. Marshalko, M. Kruglyakov, and A. Viljanen, "Estimation of the 3-D geoelectric field at the Earth's surface using spherical elementary current systems," *Annales Geophysicae*, Vol. 43, No. 1, 271–301, 2025.

[17] Wang, C., J. Xu, L. Liu, X. Xue, Q. Zhang, Y. Hao, G. Chen, H. Li, G. Li, B. Luo, Y. Zhu, and J. Wang, "Contribution of the Chinese Meridian Project to space environment research: Highlights and perspectives," *Science China Earth Sciences*, Vol. 66, No. 7, 1423–1438, 2023.

[18] Ma, X., C. Liu, and G. Liu, "The geoscience transect from Xiangshui, Jiangsu Province to Mandal, Inner Mongolia," *Acta Geologica Sinica English Edition*, Vol. 5, No. 1, 1–21, 1992.

[19] Dimmock, A. P., L. Rosenqvist, D. T. Welling, A. Viljanen, I. Honkonen, R. J. Boynton, and E. Yordanova, "On the regional variability of db/dt and its significance to GIC," *Space Weather: The International Journal of Research and Application*, Vol. 18, No. 8, e2020SW002497, 2020.

[20] Grayver, A. V., "Global 3-D electrical conductivity model of the world ocean and marine sediments," *Geochemistry, Geophysics, Geosystems*, Vol. 22, No. 9, e2021GC009950, 2021.

[21] Chave, A. D. and A. G. Jones, *The Magnetotelluric Method: Theory and Practice*, Cambridge University Press, 2012.

[22] Dong, B., Z.-Z. Wang, L.-G. Liu, L.-P. Liu, and C.-M. Liu, "Proximity effect on the induced geoelectric field at the lateral interface of different conductivity structures during geomagnetic storms," *Chinese Journal of Geophysics*, Vol. 58, No. 1, 32–40, 2015.

[23] Wang, X., C. Liu, and Z. Kang, "Effect of the Earth's lateral conductivity variations on geomagnetically induced currents in power grids," *International Journal of Electrical Power & Energy Systems*, Vol. 132, 107148, 2021.

[24] Boteler, D., "Methodology for simulation of geomagnetically induced currents in power systems," *Journal of Space Weather and Space Climate*, Vol. 4, A21, 2014.